Flexible integrated air pressure sensors for monitoring positive and negative pressure distribution

Yan Xuan[1], Takahiro Uchiyama[2*], Hiroki Ura[2], Shuji Hagiwara[2], Hiroyuki Kato[2], Sudipta Kumar Sarkar[1], Kuniharu Takei[1*]

1.Graduate School of Information Science and Technology, Hokkaido University, Sapporo 060-0814, Japan

2. Japan Aerospace Exploration Agency, Chofu 182-8522, Japan

Corresponding authors: uchiyama.takahiro@jaxa.jp (T. U.), takei@ist.hokudai.ac.jp (K. T.)

Keywords: air pressure sensors, pressure distribution, barometers, flexible sensors, laser-induced graphene, strain sensors

Abstract

Barometric pressure monitoring typically depends on conventional, rigid microelectromechanical systems (MEMS) for single-point measurements. However, applications such as fluid dynamics require mapping barometric pressure distribution to study phenomena such as pressure variations on an aircraft wing during flight. In this study, we developed a mechanically flexible, multichannel air pressure sensor sheet using laser-induced graphene (LIG). This air pressure sensor sheet is designed to be mechanically flexible, allowing it to conform to nonplanar objects. First, the crystallinity

change of LIG is studied by monitoring the bottom and top surfaces, revealing the presence of multilayered graphene and amorphous-like carbon in the formation of LIG. This explains the crystallinity change before and after the transfer process. Using LIG with optimal structures, negative and positive pressure detection is achieved, enabling its use as an air pressure sensor. Finally, as a proof-of-concept for the multichannel air pressure sensor sheet, the pressure distribution on the surface of an aircraft wing model is successfully mapped out.

Introduction

Pressure monitoring is essential for detecting noncontact barometric pressure and tactile pressure through physical contact. It is used in barometric altimeters, environmental air pressure control, and electronic skin (e-skin) applications. Additionally, extensive research has been performed on mechanically bendable, flexible pressure sensors. These sensors, known for their wide dynamic range, high sensitivity, and/or stretchable functionalities, have been developed through innovative sensor materials and structures[1-7]. Unlike conventional rigid microelectromechanical systems (MEMS) typically fabricated on silicon substrates, these flexible pressure sensors can conform to nonplanar objects owing to their mechanical flexibility. Moreover, because of their large-scale and sensor array fabrication capabilities using solution-based and/or printing techniques, flexible sensors are often applied to e-skin. This allows them to detect tactile pressure distribution, mimicking human skin functions for robotic applications [8-12]. Conversely, there are fewer reports on flexible sensors for barometric pressure monitoring compared to those for e-skin applications [13]. This may be due to the complexity of detecting both positive and negative pressures relative to the atmosphere, which often requires a membrane structure integrated with a sealed reference pressure chamber. Moreover, a single sensor is typically sufficient for barometric altimeters, and high-precision MEMS-based sensors are commercially available. Despite this, achieving barometric pressure mapping could significantly benefit aerodynamics by enabling real-time observation of pressure distribution. This would allow for monitoring air pressure on an aircraft wing for fluid dynamics studies and aircraft design improvements. Currently, to monitor pressure distribution on an aircraft wing, designed wing models incorporate stainless-steel piping inside the wing and presure taps on the surface. These tubes are connected to pressure sensors placed outside the wing for data acquisition. However, this method is limited to models because it involves drilling holes in the airframe surfaces, which is generally prohibited for actual aircraft. Additionally, the tubing arrangement inside models must be designed before construction, making it difficult to add pressure taps later if new locations need to be monitored. Response time delays owing to long tubes can also be problematic. An alternative method for determining surface pressure distribution on models is using pressure-sensitive paint (PSP) [14]. This paint emits light when exposed to excitation light, and the intensity of the emission correlates with pressure. Pressure distribution can be measured through luminescence intensity mapping. However, this method does not provide absolute pressure values; obtaining these requires a quantitative reference point, such as a pressure sensor. Additionally, measurements cannot be taken at optically inaccessible locations. Furthermore, the sensitivity of PSP is often insufficient for low-speed conditions, and the measurement results may vary depending on how the model is painted and by whom. As described, there are limitations to studying pressure distribution under various wing designs and conditions, including those of actual aircraft. In contrast, flexible air pressure sensor array sheets can be attached to nonplanar surfaces, functioning as add-on sensors simply by being attached to the target object. For instance, Chen et al. developed a barometric altimeter with a high sensitivity pressure sensor using nanoparticles on a polyethylene terephthalate (PET) film, achieving a pressure change resolution of 0.5 Pa and an altitude detection resolution of 1 m [13]. However, although the sensing part was fabricated on a flexible film, the membrane structure was realized using a bulky, rigid chamber, and only a single sensor was demonstrated. To achieve a completely flexible pressure sensor, Hu et al. developed a flexible air pressure sensor integrated with an air cavity [15]. Although they achieved a flexible air pressure sensor without needing a bulky and rigid chamber, they did not demonstrate the monitoring of air pressure distribution, which presents a challenge in integrating multiple sensors. Inspired by these findings and aiming to address the sensor array issue, we developed a fully flexible integrated multiple air pressure sensor sheet. This sheet is fabricated primarily through printing and transfer processes on PET and polydimethylsiloxane (PDMS) films. Using printing technology, multiple sensors can be easily integrated on the planar surface of the film to measure barometric pressure distribution. A key component of this air pressure sensor is a strain sensor that monitors the sensor’s deformation under pressure conditions. Laser-induced graphene (LIG) [16], which is studied widely for the sensor applications [17-20], is used in the resistive strain sensor component. During development, differences in LIG quality before and after the transfer process are addressed to resolve previous issues related to crystallinity changes during processing. After optimizing the LIG and fabrication processes, the fundamental properties of the LIG-based bending sensor are characterized. Subsequently, a study is performed on a membrane-based air pressure sensor, examining its electrical performance under positive and negative pressures and using finite element method (FEM) analyses. Finally, pressure distribution on a small aircraft wing model in uniform flow is discussed as a proof-of-concept for these integrated multichannel air pressure sensors.

Results and Discussion

The membrane-type resistive air pressure sensor was designed by laminating PDMS films with an air reference pressure chamber beneath the membrane (Figures 1a–b). The internal pressure in the chamber was maintained at approximately atmospheric pressure. Once the air pressure sensor region was formed, it was laminated onto a PET film with Ag electrodes to transmit signals to a data logger. The detailed fabrication process is explained in the Methods section and shown in Figure S1. When atmospheric pressure is lower than the reference pressure, the membrane inflates, applying tensile strain to the LIG area. Conversely, the membrane deflates when the pressure exceeds the reference, causing compressive strain in the LIG (Figure 1a). The LIG/PDMS membrane undergoes both stretching and bending owing to the inflation and deflation process. To ensure stable measurement of resistance changes in LIG even under stretching conditions, GaInSn (Galinstan), a room temperature liquid metal, was applied to the PDMS area to interconnect between the LIG and Ag electrodes on the PET film (Figure 1b).

Galinstan was dispensed using a printing tool without applying pressure from a syringe, as illustrated in Figure 1c. The syringe movement was computer-controlled. Surface tension and adhesion on the PDMS film enabled continuous patterning of Galinstan with a relatively consistent width, as depicted in Figures 1d–e. Although previous studies have discussed applying pressure [21] or using a roller-ball pen[22] to print liquid metal, this study found that neither pressure nor a complicated roller-ball structure is required to print a continuous Galinstan electrode on flexible films when using a syringe needle. The highest resolution achieved for Galinstan pattern width in this study was 570 μm using a needle with a 0.41 mm inner diameter. Finer patterns may be achievable with a smaller syringe needle. The mechanical properties of the printed Galinstan electrode on the PDMS film were subsequently characterized. First, the resistance change ratio ($\Delta R/R_0$), where R_0 (approximately 7 Ω) is the initial resistance before bending, and ΔR is the resistance change under bending conditions from R_0, was measured under tensile and compressive strain. The maximum observed $\Delta R/R_0$ was ~8%, corresponding to a change of ~0.56 Ω, which is relatively small compared to the resistance of LIG (~670 Ω). This indicates that Galinstan electrodes can be used with minimal impact on sensor response under varying bending conditions. Additionally, it was confirmed that Galinstan electrodes exhibit stability over multiple bending cycle tests (~500 cycles) under tensile (Figure 1g) and compressive (Figure 1h) strain.

Next, the crystallinity difference of LIG before and after the transfer process was analyzed using Raman spectroscopy and scanning electron microscopy (SEM) images. The detailed processes for forming LIG by laser exposure and transferring it onto PDMS are explained in the Methods section. Briefly, the thermal effect of laser exposure converts the polyimide (PI) film into porous graphene layers. Cross-section SEM images obtained after LIG formation on a polyimide (PI) film reveal two distinct layers (Figure 1i). SEM images of surface morphologies before and after removing the top layer using tape from the formed film on the PI are shown in Figures 1j and 1k, respectively. These SEM images indicate that the layers formed by laser exposure consist of a top low-density porous layer and a high-density porous (dense) layer located between the porous layer and the PI film. Raman spectroscopy confirmed the LIG layers' crystallinity by examining the 2D, G, and D peaks of the porous and dense layers on the PI (Figure 1l). The porous layer (after LIG formation on the PI) exhibits distinct 2D and G peaks, indicating the presence of multilayered graphene with defects (D peak). In contrast, the dense layer, formed after removing the porous layer using the taping method, shows broadened D and G peaks and lacks clear 2D peaks. This suggests that the dense layer resembles an amorphous carbon layer. The Raman spectroscopy results obtained after transferring LIG onto the PDMS layer (Figure 1l) align with this observation. After the transfer process, the dense layer of LIG faces up on the PDMS surface, indicating that the amorphous carbon profile observed in the Raman spectroscopy after LIG transfer to PDMS is likely owing to the initial formation of LIG on the PI film. While previous studies have noted similar Raman spectroscopy changes between graphene and amorphous carbon before and after transfer, the detailed mechanism behind this phenomenon has not been thoroughly discussed [23-25]. The findings in this study may help to understand LIG material and to realize optimal formation process without amorphous layer. If highly crystalline LIG layer without having amorphous layer can be formed, this may improve the sensor performance such as stability and reproducibility.

The fundamental electrical properties of LIG on PDMS as a bending strain sensor were characterized under tensile and compressive strain conditions induced by bending the LIG/PDMS structure. A resistive-type LIG strain sensor with Galinstan interconnect electrodes was fabricated, as depicted in Figure 2a. It confirmed that the LIG on the PI can be reproducibly and uniformly formed by this process with the sheet resistance at 23.13 ± 2.00 Ω/square (Figure S2). Here, LIG thickness was fixed ~63 μm. Due to the use of relatively large laser power (11.25 W) to realize stable and reliable sensor operation, LIG thickness could not be changed although it could be controlled at low laser power reported previously[25]. To investigate the strain effects based on structural design, the PDMS thickness (T_{PDMS}) was varied from 200 to 800 μm (Figure 2b). The formation of low- and high-porous LIGs results in electrical connectivity changes between LIG layers corresponding to mechanical deformation owing to strain. The tensile strain was applied by adjusting the bending radius, *r*. Owing to reduced electrical connectivity under tensile strain compared to the flat state, the resistance change ratio ($\Delta R/R_0$), where R_0 is the initial resistance at the flat state, and ΔR is the resistance change in the bent state from R_0, increases with decreasing bending radius (Figure 2c). Furthermore, owing to strain distribution dependent on the PDMS thickness (T_{PDMS}), thicker PDMS shows higher strain at a smaller bending radius, resulting in a larger increase in resistance compared to thinner PDMS. Conversely, when compressive strain is applied, the resistance decreases owing to improved electrical contact between LIG layers (Figure 2d). Similarly, thicker PDMS exhibits a greater decrease in resistance. The thickness dependence of the resistance change ratio is illustrated in Figure S3. These variations in resistance at different *r* and T_{PDMS} can be understood using the formula for calculating strain (ε) in a single layer.

$$\varepsilon = T_{PDMS}/2r$$

Although this formula for a single layer does not accurately extract strain values because the device structure involves two layers of LIG and PDMS, a more complex formula is required [26, 27]. It is evident that strain depends on T_{PDMS} and *r*, and these findings align with experimental results (Figures 2c–d). Importantly, these changes in resistance were primarily attributed to LIG rather than Galinstan. This is because the resistance value (R_0) of LIG is approximately 670 Ω, which is approximately 1,000 times higher than the resistance change of Galinstan under strain, rendering the resistance change of Galinstan negligible. When using elastomer-based mechanical sensors, hysteresis is another crucial parameter for sensor characterization. Figures 2e–f depict $\Delta R/R_0$ as a function of bending radius, showing continuous decrease and increase in bending radius. Although the resistance tends to decrease slightly when the sensor returns to the flat state from bending, the hysteresis is likely acceptable for an air pressure sensor. However, optimizing materials and structures could further enhance precision and speed in pressure monitoring responses. Consistent with hysteresis behaviors, cycle tests also indicate a trend of resistance decrease during bending cycles, particularly under tensile strain applications (Figures 2g–h). Importantly, despite minor resistance drift during repeated bending, sensor outputs remain relatively stable, indicating that the LIG/PDMS-based strain sensor can be used repeatedly. This stable operation is achieved by the embedding of LIG in PDMS, which protects the three-dimensional porous LIG structure under strain.

Next, a membrane-based flexible air pressure sensor was characterized. An air chamber made of PDMS was bonded over the LIG sensor (Figure 3a). The sensor design, illustrated in Figure 3b, involved varying the membrane thickness (T_m) to find the optimal structure. The membrane inflated and deflated in response to changes in barometric pressure. The membrane remains stretched during inflation and deflation, corresponding to barometric pressure changes. At positive pressure conditions (i.e., deflation), the LIG region also experiences compressive strain owing to downward bending. To verify strain distributions, finite element method (FEM) simulations were performed for negative and positive pressures. The Mooney–Rivlin 5-parameter hyperelastic model was used in these FEM simulations owing to the nonlinear behavior of the PDMS layer [28]. LIG was positioned on the top surface of the membrane, assuming the mechanical properties of LIG were equivalent to PDMS owing to unknown specific properties for LIG/PDMS.

Representative strain distributions calculated via FEM are depicted in Figures 3c–d, aligning with the expected results. To quantitatively discuss sensor output corresponding to strain, the average strain across the entire LIG region (designed to be 5 mm wide and 0.1 mm deep) was calculated. Under negative pressure conditions characterized by membrane inflation and upward bending of LIG, significant tensile strain was observed in the LIG (Figure 3e). Strain changes were observed as expected by varying T_m. However, there was a significant difference in the trend of strain changes depending on T_m under positive pressure conditions (Figure 3f). With a thicker T_m structure, the compressive strain was consistently applied regardless of barometric pressure, whereas with a thinner T_m, the strain varied from compressive to tensile. This difference in strain reflects a balance between the tensions caused by deflation and the compressions owing to bending.

To verify strain changes under different pressures, the resistance change ratio $\Delta R/R_0$ was measured, where R_0 is the initial resistance at atmospheric pressure (the same as the air chamber), and ΔR is the resistance change at specific pressures relative to R_0. This was assessed across applied positive and negative pressures and varying T_m (Figure 3g–h). In both negative and positive pressure scenarios, the trends in resistance changes closely mirrored the average strain changes extracted from FEM simulations. Figures 3i–j demonstrate the dependence on membrane thickness under different pressure conditions. For effective air pressure sensor changes, positive and negative pressure changes must result in consistent resistance changes. Based on the results presented in Figures 3i–j, it was determined that T_m should be greater than 500 μm. Furthermore, a T_m of 800 μm was selected for the air pressure sensor in this study to achieve higher sensitivity. In this design, sensitivity calculated from linear fitting of $\Delta R/R_0$ per applied pressure is ~10.2 %/kPa for negative pressures ranging from 0 to −30 kPa and ~−0.55 %/kPa for positive pressures from 0 to 30 kPa. Subsequently, hysteresis and cycle tests were performed by alternately applying positive and negative pressures. The membrane-based sensor exhibited minimal hysteresis (Figures 3k–l) and some response fluctuations during repeated measurements (Figures 3m–n). To explore the sensor design further for increasing sensitivity, average strain distribution in the membrane at different pressures was simulated using FEM as a function of the air chamber depth (Figure S4). The results showed that the deeper the chamber, the lower the strain at negative pressure and the higher the strain at positive pressures. To achieve high sensitivity at both negative and positive pressure, this study decided to adopt a design with an air chamber depth of 1.0 mm.

The sensor response to other environmental factors was briefly investigated. Changes in temperature and humidity, common variables in environmental applications, were measured for both the bending and air pressure sensors. As expected, the bending sensor exhibited an increase in resistance with rising temperature owing to the thermal expansion of PDMS (Figure 4a), consistent with previous studies on the LIG/PDMS structure [29]. Furthermore, the sensor exhibits a slight dependence on humidity, showing approximately a −2% change from relative humidity (RH) 40% to 80% (Figure 4b). However, this change is negligible compared to the resistance change ratio of the bending sensor. With increasing temperature, the air pressure sensor's resistance increases approximately 4 times more than that of the bending sensor. This effect is likely attributed to the thermal expansion of air in the chamber and the expansion of the PDMS membrane (Figure 4c). Finally, the air pressure sensor demonstrates a similar response to humidity as the bending sensor (Figure 4d), indicating that the resistance change owing to humidity is influenced by interactions between LIG and water molecules rather than mechanical deformation. Another important parameter is the change in sensitivity at different temperature and humidity. Although humidity change and systematic temperature dependence study could not be conducted due to the measurement setup limitation, the sensor output shows a higher sensitivity for both negative and positive pressure at higher temperature (Figure S5). As a systematic study has not yet been demonstrated, the mechanism of the change in sensitivity with respect to temperature is not understood and requires further work. While humidity changes are largely negligible for the application, temperature responses may require compensation, possibly through integrating a temperature sensor with this air pressure sensor in future applications. However, this aspect is beyond the scope of this study, which focuses on developing a planar integrated air pressure sensor sheet.

To validate this sensor as an air pressure sensor, it was integrated with an analog–digital (AD) converter, a microcontroller, and a low-energy Bluetooth (BLE) module to measure environmental pressure during a flight from New Chitose Airport (CTS) to Haneda International Airport (HND) in Japan (Figures 4e–f). A small lithium-ion battery provided power. The sensor outputs were transmitted to a smartphone, where data were displayed and saved using a developed app. For reference, environmental pressure was simultaneously measured using the barometer function of an iPhone 13. Despite a slight drift observed in the low pressure range during the flight, the flexible air pressure sensor exhibited nearly identical changes compared to the reference result (Figure 4g). This minor deviation at low pressure could be attributed to drift in LIG performance and/or slight air leakage from the chamber to the atmosphere over extended periods of negative pressure because PDMS is not a perfect air barrier. To validate the reproducibility of these findings, measurements were repeated four times, each showing a consistent trend. In addition, to observe the effect of long-term air leakage, the sensor was kept in a chamber at – 5 kPa for about 7 hours and measured the resistance of the sensor continuously (Figure S6). Based on the results, about 1 hour after the start of measurement, a large decrease in resistance was observed, mainly due to air leakage from the chamber. However, after 1 hour, the resistance value is stable for more than 6 hours. This air leakage may be dependent on the air pressure difference between the air chamber and the environment. Addressing this phenomenon will be crucial for enhancing the long-term monitoring performance of the air pressure sensor in future.

Finally, a 1 × 5 array of flexible air pressure sensors was integrated onto a PET film as a proof-of-concept to monitor air pressure distribution. The integrated air pressure sensor sheet was then attached to the surface of a small aircraft wing model to observe changes in surface pressure distribution under uniform flow conditions simulating takeoff and landing (Figures 5a–b). The five sensors were positioned along the direction of airflow. The angle θ of the wing relative to the airflow was varied to create differences in pressure distribution across the sensor array (Figure 5c). First, the pressure distribution corresponding to the angle θ was measured using commercial sensors via pressure taps on the model surface tubes before attaching the air pressure sensor sheet. Once the pressure distribution was confirmed, the air pressure sensor sheet was attached to the model, with specific locations detailed in Figure 5d. The five sensors were designated as channels #1 to #5. Figure 5e illustrates the resistance changes of the air pressure sensor sheet alongside the pressure changes measured by the commercial sensor at each angle θ. At $\theta = 0$, the flow accelerates over the curved surface of the model, leading to a decrease in pressure in that region according to Bernoulli's principle. As θ increases, pressure on the wing's pressure side rises, resulting in lift generation. Owing to sensor sensitivity variations, quantitative pressure values could not be directly extracted from the air pressure sensor on this occasion. It should be noted that channel #2 exhibited lower sensitivity than the others, resulting in minimal resistance change. However, the trends in pressure changes (both positive and negative relative to the base reference pressure of the chamber) closely aligned with those recorded by the commercial sensors. Importantly, the air pressure sensor sheet accurately identified positions where pressure transitions occurred from positive to negative along the cross-section where the sensors were installed and the angles θ where pressure shifted from negative to positive at specific sensor positions. In essence, the sensor effectively captured variations in pressure distribution corresponding to changes in aircraft attitude during takeoff and landing conditions. It is noteworthy that the pressure sensor has no sensitivity to weak air flow using a small fan (air flow velocity is unknow), which causes almost no pressure change on the surface, concluding that the pressure distribution shown in Figure 5e is caused by the air pressure surrounding the wing model. While challenges remain, such as pressure value extraction and sensor uniformity, the successful demonstration of the flexible air pressure sensor sheet as an add-on sensor is a significant achievement not realized in previous studies of flexible air pressure sensors.

Conclusion

In this study, we developed a printed and integrated flexible air pressure sensor sheet designed to monitor positive and negative pressure distribution as an add-on system by attaching the sensor sheet to a target object. Before discussing the air pressure sensor, we investigated the crystallinity difference of LIG formed on the PI film. We uncovered why the amorphous-like carbon was observed after transferring LIG from PI to the elastomer polymer. This issue had not been addressed despite prior reports of crystallinity differences [23-25]. Using the transferred LIG in the PDMS, a bending sensor to establish fundamental properties for the air pressure sensor was characterized. The sensor demonstrated resistance increase under tensile strain and decrease under compressive strain, consistent with the sensing mechanism of LIG-based strain sensors. Subsequently, the flexible air pressure sensor by incorporating an air chamber onto the LIG/PDMS membrane was characterized. Based on both FEM simulations and experimental findings, it was determined that the membrane thickness should be greater than 500 μm to consistently achieve positive and negative resistance changes corresponding to negative and positive pressures, respectively. The sensor was used to monitor environmental pressure in an aircraft cabin during flight to validate its capability as an air pressure sensor. Furthermore, as a proof-of-concept, five flexible air pressure sensors were integrated onto a PET film and attached to a small aircraft wing model to observe pressure distribution on the wing surface in a uniform wind flow. The successful mapping of pressure distribution using the air pressure sensor sheet was confirmed by comparing it with embedded wing pressure sensors as references. Although this study used the LIG/PDMS membrane structure for the pressure sensor because of its ease of fabrication and integration process, other membrane materials can also be used instead of PDMS. However, it is important to note that the membrane must generate strain under both negative and positive pressures, and the sensor structure needs to be designed as thin as possible for the aircraft applications. Despite numerous challenges for practical applications, such as stability and performance uniformity, an integrated, flexible air pressure sensor is promising for future applications in the Internet of Things (IoT).

Experimental Methods

Fabrication process:

The flexible air pressure sensor was fabricated using the process outlined in Figure S1. Initially, a 125-μm-thick PI film was scanned with a CO_2 laser (VLS2.30, UNIVERSAL Laser System) operating at 11.25 W power (45% laser power, 30% laser speed) (Figure S1(1)). The thermal effect of the laser on the PI film resulted in carbonization of the exposed areas, forming multilayered defective graphene and amorphous-like carbon layers (Figure S1(2)) [24, 25]. PDMS solution, consisting of a 10:1 weight ratio of PDMS base solution and curing agent, was spin-coated over the LIG/PI film and cured at 90°C for 2 h (Figure S1(3)). Following curing, the PDMS film was peeled off, transferring the LIG from the PI film to the PDMS film (Figure S1(4)). Galinstan electrodes were then printed onto the transferred LIG on the PDMS to interconnect the LIG-based strain sensor (Figure S1(5)). It should be noted that other soft electrodes may be used to achieve good electrical connection between LIG and Ag electrodes provided that the adhesion and softness of the electrodes are sufficient to withstand the high wind speeds and pressures in aircraft applications. Subsequently, a PDMS cavity, fabricated using a mold, was bonded to the backside of the LIG/PDMS film using PDMS solution as adhesive glue (Figure S1(6)). After an initial cure at room temperature for over 8 h to prevent shrinkage or expansion of the LIG/PDMS film, a second curing step at 90°C for 1 h was performed to ensure secure bonding. Ag electrodes were screen-printed onto a PET film to serve as electrical connections between the sensor/Galinstan and a data logger. Both surfaces were first treated with oxygen plasma to achieve strong bonding between the PDMS chamber and the Ag/PET film. After oxygen plasma treatment, the Ag/PET film was immersed in a 1wt% APTES solution for 1 h at room temperature. After drying, the Ag/PET film was laminated over the LIG/PDMS structure to achieve a strong chemical bond (Figure S1(7)).

For this bonding, the Ag/PET film did not completely cover over Galinstan region due to difficulty to align perfectly between Galinstan pattern and the Ag/PET film. To realize highly stable sensor system, this exposed Galinstan also needs to be protected by some passivation layer in the future. Finally, the air pressure sensor was connected to a data logger for signal acquisition and analysis. All experiments were confirmed by at least three samples for each condition.

FEM simulation

FEM simulation was performed using COMSOL Multiphysics 6.2. The sensor geometry was modeled based on the dimensions illustrated in Figure 3b. A 2D model was created, simplifying the representation of LIG to optimize computational efficiency while maintaining accuracy. Material properties for PDMS were selected according to established literature values [28]. The Mooney–Rivlin 5-parameter model was applied for PDMS [28], with the parameters derived from the following equations:

$$C_{10} = 5.12 \times 10^3 - 1.28 \times 10^5 n + 8.02 \times 10^5 n^2$$

$$C_{20} = 4.3 \times 10^3 - 1.09 \times 10^5 n + 6.92 \times 10^5 n^2$$

$$C_{11} = -1.56 \times 10^3 + 4.07 \times 10^4 n - 2.65 \times 10^5 n^2$$

$$C_{01} = -4.8 \times 10^3 + 1.19 \times 10^5 n - 7.37 \times 10^5 n^2$$

$$C_{02} = 3.44 \times 10^3 - 8.6 \times 10^4 n + 5.39 \times 10^5 n^2$$

The calculation used $n = 0.1$, resulting in $C_{10} = 340$, $C_{20} = 320$, $C_{11} = -140$, $C_{01} = -270$, $C_{02} = 230$. Fixed boundary conditions were applied to the sensor's bottom and sides. A uniform pressure load ranging from −40 to 40 kPa was applied to the sensor surface to simulate real operating conditions. The simulation was configured as a static structural analysis using default COMSOL solver settings, with nonlinear analysis options enabled to accommodate large deformations. The strain analysis focused on a specific region of the sensor surface measuring 100 μm × 5 mm. Postprocessing the simulation results involved extracting the strain distribution and calculating the average strain value across the defined area.

Pressure distribution monitoring on the wing surface:

(1) Test Facilities:

The JAXA 2 m × 2 m low-speed wind tunnel (JAXA-LWT2) was used for a proof-of-concept to monitor air pressure distribution. This wind tunnel is an atmospheric pressure closed-circuit system with solid walls. The test section of the tunnel features a square cross-section measuring 2 m in height, 2 m in width, and 4 m in length. Capable of generating uniform flows up to 67 m/s, equivalent to typical aircraft takeoff and landing speeds, the freestream speed for this experiment was specifically set at 60 m/s. One test was performed under a fixed flow velocity using a pitch–pause mode. In this mode, the model's angle θ relative to the airflow in the test section is set to a desired value by rotating the model. Data are then collected in that orientation, and the process is repeated for different θ angles as needed. The test was repeated three times, with wind tunnel stops and restarts between each iteration.

The test was performed using a NACA 0012 quasi-2-dimensional wing model [30]. The model used in the experiment had dimensions of 1,000 mm in span, 400 mm in chord, and 48 mm in thickness, positioned on the floor of the wind tunnel test section. This model shape is a global standard in the aerospace industry and is commonly employed for basic research and various applications. It featured 59 static pressure taps, with 35 aligned along the chord direction, positioned at 400 mm height from the floor. These pressure taps were connected via pressure tubes to commercial pressure sensors (Scanivalve Corp., ZOC22B and ZOC33) located outside the wind tunnel.

(2) Data acquisition and data processing:

An air pressure sensor sheet was installed along the pressure tap line of the wing model, positioned at 400 mm from the floor, and compared with a commercial sensor. The air pressure sensor was connected to a power supply (National Instruments Corp., cDAQ-9178 and NI-9265) and a voltage measuring device (National Instruments Corp., PXI-1033 and PXI-4462), with a constant current applied during testing.

To obtain data under specific conditions, voltage values from the sensor were recorded at 100 Hz for 10 s. The data underwent low-pass filtering at 1 Hz, and the time-averaged result was considered the voltage value for that condition. The sensor resistance was then derived from the current and voltage readings. A reference resistance value was calibrated against the resistance at standard atmospheric pressure, which served as the reference pressure, using measurements from the pressure taps. The difference in resistance values for each condition from the reference was determined using the average of the three tests, with the standard deviation used as an error bar. These values were then compared to the differences from the reference pressure obtained from the commercial sensor. Despite slight positional variations between each sensor channel and pressure tap, comparisons were performed using linear interpolation on the pressure tap data. Average data and error bars for the flexible pressure sensor were ploted with the sample number N=3.

ASSOCIATED CONTENT

Supporting Information. Supporting Information is available free of charge at.

Fabrication process and resistance change ratio of functions of bending radius and PDMS thickness.

AUTHOR INFORMATION

Corresponding Author

*Takahiro Uchiyama, uchiyama.takahiro@jaxa.jp

*Kuniharu Takei, takei@ist.hokudai.ac.jp

Author Contributions

T. U, H. U. H. K., and K. T. conceived the concept; All authors designed the research and experiments; Y. X., T. U., H. U., S. H., S. K. S. performed the experiments and analysis on all device sections; All authors contributed to discussions, providing insights, analysis, and manuscript writing.

Notes

The authors declare no competing financial interest.

Acknowledgements

This work was partially supported by JST AIP Accelerated Program (No. JPMJCR21U1), JSPS KAKENHI (Grant No. JP22H00594, JP24H00887), the Murata Science Foundation, and the Takeda Science Foundation.

References

(1) Someya, T.; Kato, Y.; Sekitani, T.; Iba, S.; Noguchi, Y.; Murase, Y.; Kawaguchi, H.; Sakurai, T. Conformable, flexible, large-area networks of pressure and thermal sensors with organic transistor active matrixes. *Proc. Natl. Acad. Sci. U.S.A.* **2005**, *102*, 12321-12325.

(2) Lee, S.; Franklin, S.; Hassani, F. A.; Yokota, T.; Nayeem, M. O. G.; Wang, Y.; Leib, R.; Cheng, G.; Franklin, D. W.; Someya, T. Nanomesh Pressure Sensor for Monitoring Finger Manipulation without Sensory Interence. *Science* **2020**, *370*, 966-970.

(3) Wang, M.; Tu, J.; Huang, Z.; Wang, T.; Liu, Z.; Zhang, F.; Li, W.; He, K.; Pan, L.; Zhang, X.; et al. Tactile Near-Sensor Analogue Computing for Ultrafast Responsive Artificial Skin. *Adv. Mater.* **2022**, *34*, e2201962.

(4) Takei, K.; Takahashi, T.; Ho, J. C.; Ko, H.; Gillies, A. G.; Leu, P. W.; Fearing, R. S.; Javey, A. Nanowire active-matrix circuitry for low-voltage macroscale artificial skin. *Nat. Mater.* **2010**, *9* (10), 821-826.

(5) Wang, S.; Xu, J.; Wang, W.; Wang, G. N.; Rastak, R.; Molina-Lopez, F.; Chung, J. W.; Niu, S.; Feig, V. R.; Lopez, J.; et al. Skin Electronics From Scalable Fabrication of an Intrinsically Stretchable Transistor Array. *Nature* **2018**, *555*, 83-88.

(6) Dagdeviren, C.; Su, Y.; Joe, P.; Yona, R.; Liu, Y.; Kim, Y. S.; Huang, Y.; Damadoran, A. R.; Xia, J.; Martin, L. W.; et al. Conformable amplified lead zirconate titanate sensors with enhanced piezoelectric response for cutaneous pressure monitoring. *Nature communications* **2014**, *5*, 4496. DOI: 10.1038/ncomms5496.

(7) Lee, Y.; Myoung, J.; Cho, S.; Park, J.; Kim, J.; Lee, H.; Lee, Y.; Lee, S.; Baig, C.; Ko, H. Bioinspired Gradient Conductivity and Stiffness for Ultrasensitive Electronic Skins. *ACS Nano* **2021**, *15*, 1795-1804.

(8) Cho, Y.; Kim, T.; Kim, G.; Do, H. W.; Kim, S. R.; Park, J. W.; Myoung, J. M.; Shim, W. Three-Dimensional Touch Device with Two Terminals. *Adv. Mater.* **2023**, *35* (42), e2305697. DOI: 10.1002/adma.202305697 From NLM PubMed-not-MEDLINE.

(9) Zhang, Y.; Yang, J.; Hou, X.; Li, G.; Wang, L.; Bai, N.; Cai, M.; Zhao, L.; Wang, Y.; Zhang, J.; et al. Highly Stable Flexible Pressure Sensors with a Quasi-Homogeneous Composition and Interlinked Interfaces. *Nat. Commun.* **2022**, *13*, 1317.

(10) Harada, S.; Kanao, K.; Yamamoto, Y.; Arie, T.; Akita, S.; Takei, K. Fully Printed Flexible Fingerprint-like Three-Axis Tactile and Slip Force and Temperature Sensors for Artificial Skin. *ACS Nano* **2014**, *8*, 12851-12857.

(11) Li, Y.; Matsumura, G.; Xuan, Y.; Honda, S.; Takei, K. Stretchable Electronic Skin Using Laser-Induced Graphene and LIquid Metal With an Action Recognition System Powered by Machine Learning. *Adv. Funct. Mater.* **2024**, 2313824. DOI: 10.1002/adfm.202313824.
(12) Lei, M.; Feng, K.; Ding, S.; Wang, M.; Dai, Z.; Liu, R.; Gao, Y.; Zhou, Y.; Xu, Q.; Zhou, B. Breathable and Waterproof Electronic Skin with Three-Dimensional Architecture for Pressure and Strain Sensing in Nonoverlapping Mode. *ACS Nano* **2022**, *16*, 12620-12634.
(13) Chen, M.; Luo, W.; Xu, Z.; Zhang, X.; Xie, B.; Wang, G.; Han, M. An Ultrahigh Resolution Pressure Sensor Based on Percolative Metal Nanoparticle Arrays. *Nat. Commun.* **2019**, *10*, 4024. From NLM PubMed-not-MEDLINE.
(14) Nakakita, K.; Kurita, M.; Mitsuo, K.; Watanabe, S. Practical Pressure-Sensitive Paint Measurement System for Industrial Wind Tunnels at JAXA. *Measurement Sci. and Technol.* **2006**, *17*, 359-366.
(15) Hu, F.; Chen, Z.; Xu, B.; Wang, Q.; Huang, X.; Yang, H.; Liang, H.; Chen, G.; Zheng, J.; Hu, X.; et al. Waterproof, Anti‐Impacted, and Ultrathin Carbon‐Based Air Pressure Sensors Toward Aerodynamic Tests on High‐Speed Trains. *Adv. Eng. Mater.* **2022**, *24*, 2101781.
(16) Lin, J.; Peng, Z.; Liu, Y.; Ruiz-Zepeda, F.; Ye, R.; Samuel, E. L.; Yacaman, M. J.; Yakobson, B. I.; Tour, J. M. Laser-Induced Porous Graphene Films from Commercial Polymers. *Nat. Commun.* **2014**, *5*, 5714.
(17) Lu, Y.; Yang, G.; Wang, S.; Zhang, Y.; Jian, Y.; He, L.; Yu, T.; Luo, H.; Kong, D.; Xianyu, Y.; et al. Stretchable Graphene–Hydrogel Interfaces for Wearable and Implantable Bioelectronics. *Nat. Electron.* **2023**, *7*, 51-65.
(18) Yang, Y.; Song, Y.; Bo, X.; Min, J.; Pak, O. S.; Zhu, L.; Wang, M.; Tu, J.; Kogan, A.; Zhang, H.; et al. A Laser-Engraved Wearable Sensor for Sensitive Detection of Uric Acid and Tyrosine in Sweat. *Nat. Biotech.* **2019**, *38*, 217-224.
(19) Babatain, W.; Buttner, U.; El-Atab, N.; Hussain, M. M. Graphene and Liquid Metal Integrated Multifunctional Wearable Platform for Monitoring Motion and Human-Machine Interfacing. *ACS Nano* **2022**, *16*, 20305-20317.
(20) Luong, D. X.; Subramanian, A. K.; Silva, G. A. L.; Yoon, J.; Cofer, S.; Yang, K.; Owuor, P. S.; Wang, T.; Wang, Z.; Lou, J.; et al. Laminated Object Manufacturing of 3D-Printed Laser-Induced Graphene Foams. *Advanced materials* **2018**, *30* (28), e1707416. DOI: 10.1002/adma.201707416.
(21) Neumann, T. V.; Dickey, M. D. Liquid Metal Direct Write and 3D Printing: A Review. *Adv. Mater. Technol.* **2020**, *5*, 2000070.

(22) Zheng, Y.; Zhang, Q.; Liu, J. Pervasive Liquid Metal Based Direct Writing Electronics With Roller-Ball Pen. *AIP Adv.* **2013**, *3*, 112117.
(23) Liu, J.; Wu, D.; Liu, C.; Wang, Q.; Wang, H. Full‐Range On‐Body Strain Sensor of Laser‐Induced Graphene Embedded in Thermoplastic Elastomer via Hot Pressing Transfer for Monitoring of the Physiological Signals. *Adv. Mater. Technol.* **2024**, *9*, 2301658.
(24) Wakabayashi, S.; Arie, T.; Akita, S.; Nakajima, K.; Takei, K. A Multitasking Flexible Sensor via Reservoir Computing. *Adv. Mater.* **2022**, *34*, 2201663.
(25) Xu, K.; Fujita, Y.; Lu, Y.; Honda, S.; Shiomi, M.; Arie, T.; Akita, S.; Takei, K. A Wearable Body Condition Sensor System with Wireless Feedback Alarm Functions. *Adv. Mater.* **2021**, *33*, e2008701.
(26) Harada, S.; Honda, W.; Arie, T.; Akita, S.; Takei, K. Fully Printed, Highly Sensitive Multifunctional Artificial Electronic Whisker Arrays Integrated with Strain and Temperature Sensors. *ACS Nano* **2014**, *8*, 3921-3927.
(27) Suo, Z.; Ma, E. Y.; Gleskova, H.; Wagner, S. Mechanics of rollable and foldable film-on-foil electronics. *Applied Physics Express* **1999**, *74* (8), 1177-1179.
(28) Zulkifli, N. A.; Moon, G. D.; Hyun, D. C.; Lee, S. Comprehensive Constitutive Modeling and Analysis of Multi-Elastic Polydimethylsiloxane (PDMS) for Wearable Device Simulations. *Sc. Rep.* **2023**, *13*, 18413.
(29) Li, Y.; Nakamura, H.; Lee, D. H.; Qin, Y.; Xuan, Y.; Takei, K. Temperature Coefficient of Resistance of Transferred Laser-Induced Graphene. *ACS Appl. Electron. Mater.* **2024**, *6*, 4630-4634.
(30) Abbott, I. H.; von Doenhoff, A. E. Theory of Wing Sections. *Dover Publications* **1959**.

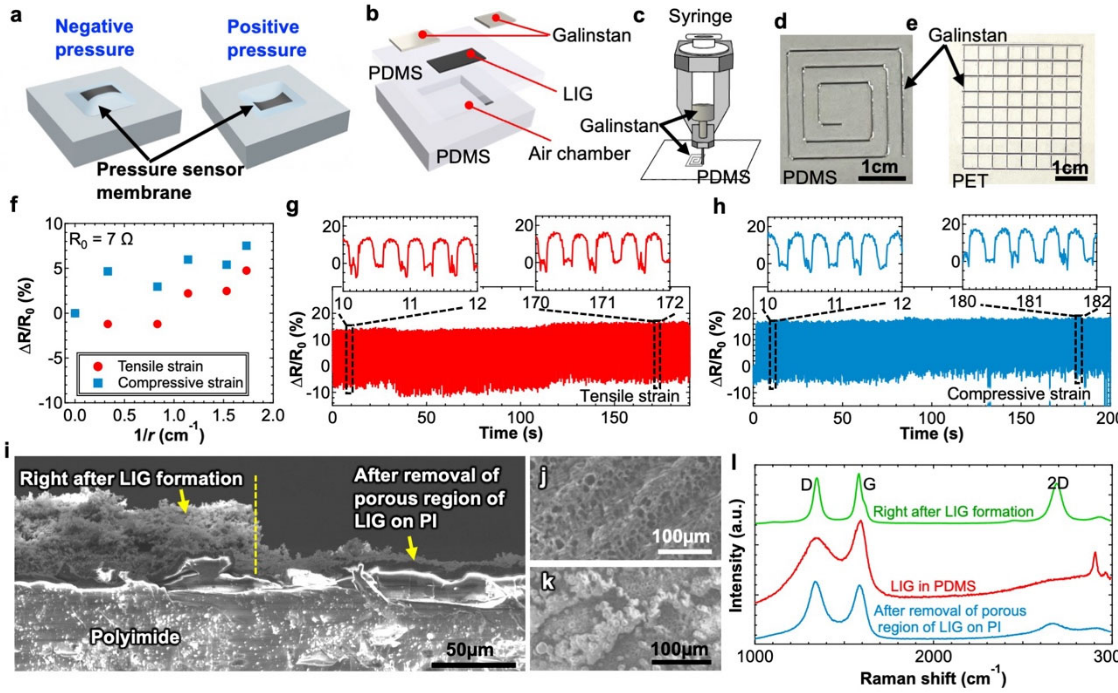

Figure 1. (a) Schematic images of the flexible air pressure sensor at negative and positive pressure. (b) Structure of the air pressure sensor. (c) Galinstan printing setup image. Photographs of the results of Galinstan printing with different patterns on (d) PDMS and (e) PET films. (f) Resistance change ratio of Galinstan as a function of bending radius *r* during tensile and compressive strain applications. Cycle tests performed under (g) tensile strain and (h) compressive strain conditions applied to the Galinstan electrode. (i) Cross-section SEM image comparing before and after removal of the porous region of LIG on PI. SEM images of the surface morphology of (j) the porous LIG after formation and (k) the dense layer remaining after removing the porous LIG region. (l) Raman spectroscopy results at three stages of LIG: after LIG formation, LIG in PDMS after transfer, and after removal of the porous LIG region on PI (plots from top to bottom).

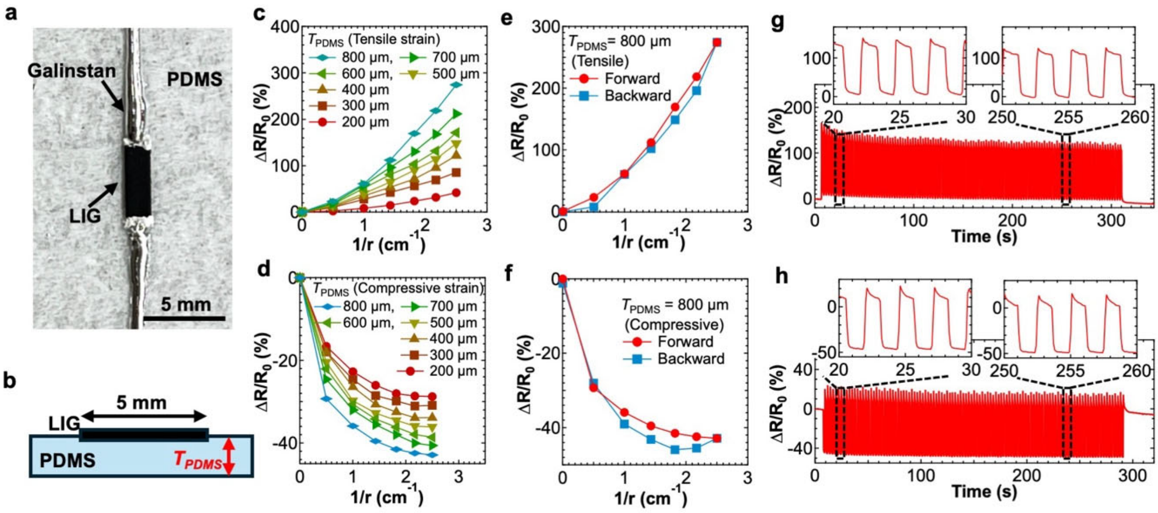

Figure 2. Bending sensor characteristics. (a) Photo of the top view and (b) cross-sectional schematic image of the bending sensor. The resistance change ratio as functions of bending radius r and PDMS thickness T_{PDMS} under (c) tensile strain and (d) compressive strain conditions. Hysteresis behaviors under (e) tensile and (f) compressive strain conditions. Cycle tests performed using 800-μm-thick PDMS under (g) tensile strain and (h) compressive strain conditions

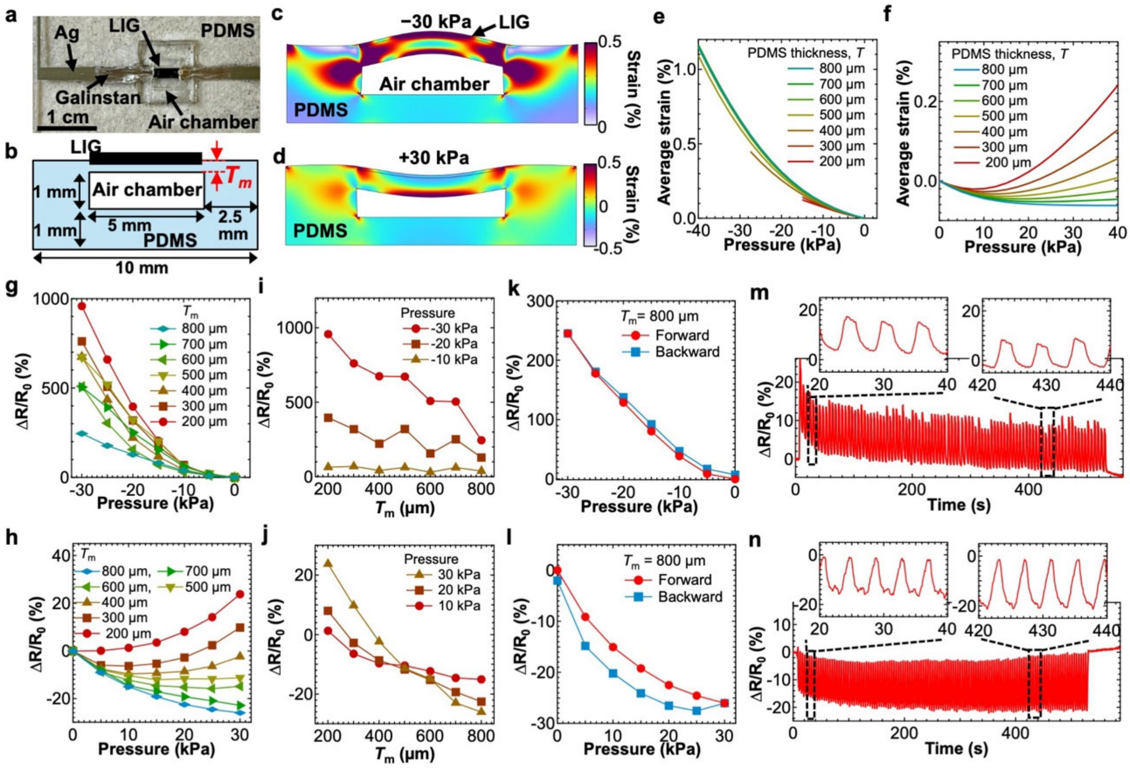

Figure 3. Flexible air pressure sensor characteristics. (a) Photo and (b) cross-sectional schematic image of the flexible air pressure sensor. Strain distribution calculated by FEM at (c) −30 kPa and (d) +30 kPa environmental pressure. Average strain in the LIG region calculated by FEM at (e) negative and (f) positive pressures with different PDMS thicknesses. Resistance change ratio as a function of pressure at (g) negative and (h) positive pressure applications with different PDMS thicknesses. Resistance change ratio at different PDMS thicknesses under (i) negative and (j) positive pressures. Hysteresis behaviors observed during (k) negative and (l) positive pressure applications. Cycle tests performed under (m) negative and (n) positive pressure applications.

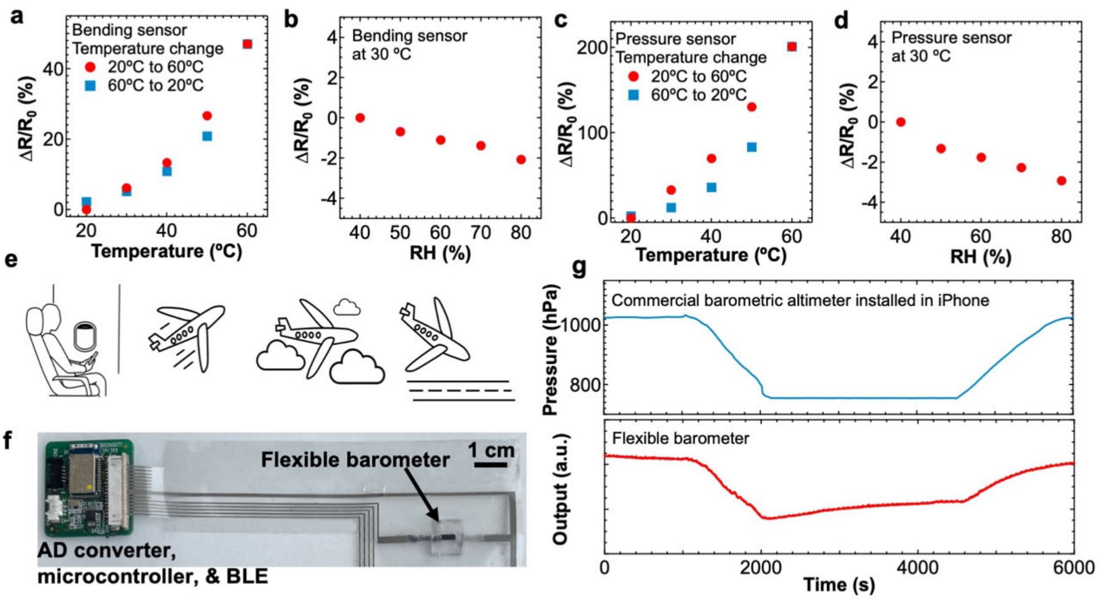

Figure 4. Resistance change ratio of the bending sensor at different (a) temperatures and (b) relative humidity. Resistance change ratio of the air pressure sensor at different (c) temperatures and (d) relative humidity. (e) Schematic of barometric pressure monitoring test. (f) Flexible air pressure sensor integrated with BLE and microcomputer modules for barometric pressure monitoring in an aircraft during flight. (g) Barometric pressure monitoring results of the commercial sensor (top) and the flexible air pressure sensor (bottom).

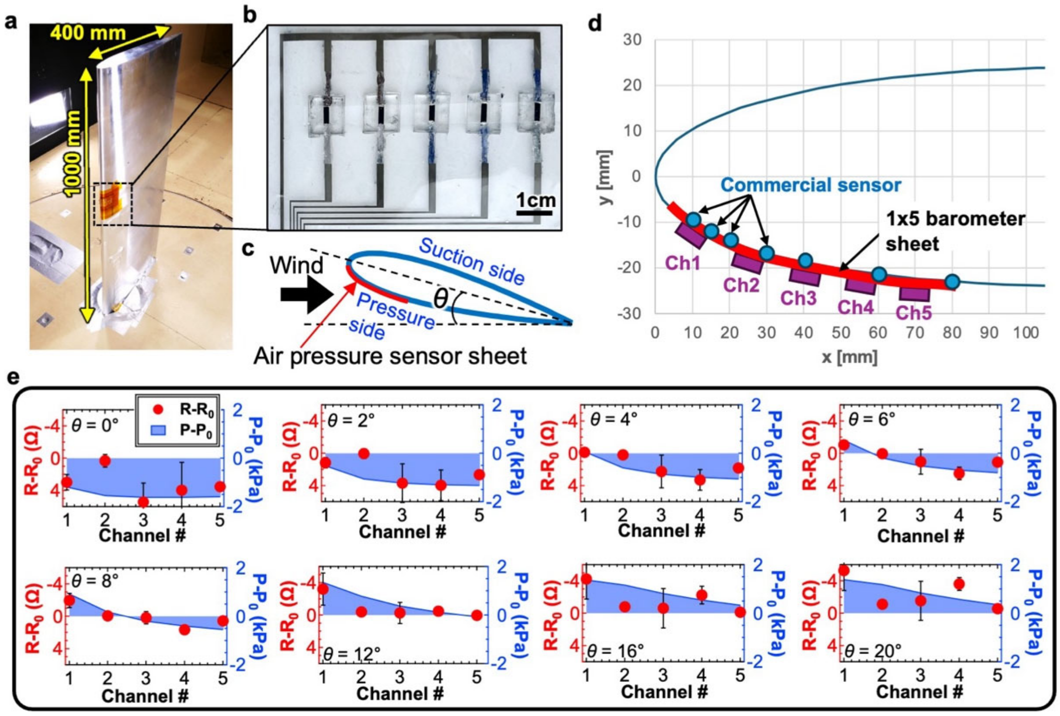

Figure 5. Photos of (a) a wing model with the integrated, flexible air pressure sensor sheet and (b) a five air pressure sensors-integrated sheet. (c) Definition of angle θ. (d) Locations of the air pressure sensor sheet on the wing and commercial sensors in the wing. (e) Resistance change and pressure difference at different angles θ from 0° to 20° (N=3).

ToC

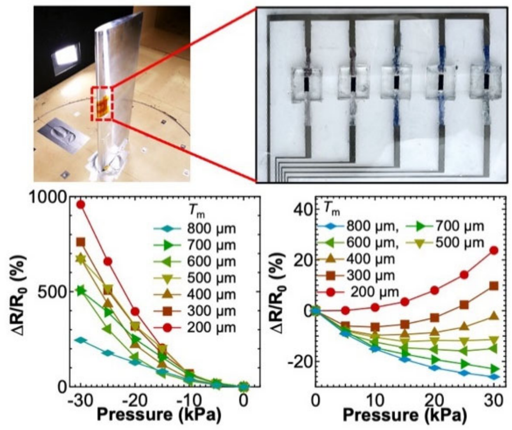

1000
500
0
-30
-20
-10
0
T_m
800 µm
700 µm
600 µm
500 µm
400 µm
300 µm
200 µm
ΔR/R₀ (%)
Pressure (kPa)
40
20
0
-20
0
10
20
30
T_m
800 µm,
700 µm
600 µm,
500 µm
400 µm
300 µm
200 µm
ΔR/R₀ (%)
Pressure (kPa)